Inorganic Chemistry

pubs.acs.org/IC Article

Spectroscopic Investigation of a Metal–Metal-Bonded Fe_6 Single-Molecule Magnet with an Isolated $S = {}^{19}/_{2}$ Giant-Spin Ground State

Joscha Nehrkorn, Samuel M. Greer, Brian J. Malbrecht, Kevin J. Anderton, Azar Aliabadi, J. Krzystek, Alexander Schnegg, Karsten Holldack, Carmen Herrmann, Theodore A. Betley,* Stefan Stoll,* and Stephen Hill*

Cite This: *Inorg. Chem.* 2021, 60, 4610−4622 Read Online

ACCESS | Metrics & More | Article Recommendations | Supporting Information

ABSTRACT: The metal−metal-bonded molecule $[Bu_4N][(^{H}L)_2Fe_6(dmf)_2]$ (Fe_6) was previously shown to possess a thermally isolated spin $S = {}^{19}/_{2}$ ground state and found to exhibit slow magnetization relaxation below a blocking temperature of ∼5 K [*J. Am. Chem. Soc.* **2015**, *137*, 13949−13956]. Here, we present a comprehensive spectroscopic investigation of this unique single-molecule magnet (SMM), combining ultrawideband field-swept high-field electron paramagnetic resonance (EPR) with frequency-domain Fourier-transform terahertz EPR to accurately quantify the spin Hamiltonian parameters of Fe_6. Of particular importance is the near absence of a 4th-order axial zero-field splitting term, which is known to arise because of quantum mechanical mixing of spin states on account of the relatively weak spin−spin (superexchange) interactions in traditional polynuclear SMMs such as the celebrated Mn_{12}-acetate. The combined high-resolution measurements on both powder samples and an oriented single crystal provide a quantitative measure of the isolated nature of the spin ground state in the Fe_6 molecule, as well as additional microscopic insights into factors that govern the quantum tunneling of its magnetization. This work suggests strategies for improving the performance of polynuclear SMMs featuring direct metal−metal bonds and strong ferromagnetic spin−spin (exchange) interactions.

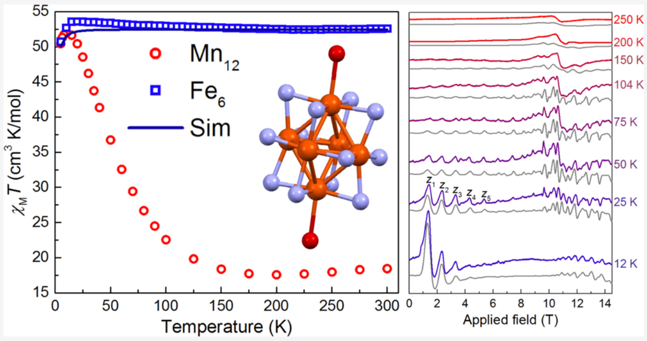

INTRODUCTION

In the field of molecular nanomagnetism, much effort has focused on achieving ground states with giant magnetic moments (either nominally pure spin, S, or coupled spin−orbital, J),[1−4] as these are advantageous for many potential applications. For example, a high degeneracy is important for magnetic refrigeration based on the magnetocaloric effect.[5] A large-spin ground state with minimal zero-field splitting (ZFS) satisfies this requirement. Meanwhile, the large Hilbert space spanned by the $2S + 1$ projection (M_S) states associated with a giant spin can potentially be harnessed for quantum information processing (QIP), wherein a single molecule can encode multiple qubits.[6,7] Referred to as a "qudit"—the generalization to d levels of a two-level system—such a molecule can encode information equivalent to $n = \log_2 d$ qubits, where $d = (2S + 1)$.[6,8] Proposals also exist that leverage these additional computational resources for creating molecular qubits/qudits with embedded error correction.[8,9] Single-molecule magnets (SMMs) are perhaps the most widely studied subgroup of molecular nanomagnets.[10] They display slow relaxation, or blocking of their magnetization that is of a purely molecular origin, i.e., they can retain their magnetization below a characteristic blocking temperature, T_B.[11] Several potential applications for these fascinating molecules have been proposed,[6,12] the most obvious being as molecular-scale memory storage units for classical computing.

SMMs containing multiple magnetic ions are often successfully described according to the giant spin approximation, which considers only the anisotropy within the ground state spin multiplet.[10,13] Achieving both a large spin and the desired strong magnetic anisotropy in the same molecule represents a formidable synthetic challenge.[14,15] Crucially, for all of the above-mentioned applications, the ground spin multiplet should be well isolated from excited states. However, in most polymetallic cases, the magnetic ions are coupled via superexchange interactions which, because of their indirect nature, are inherently weak.[16] Hence, the resulting separation between spin multiplets is often comparable to the ZFS within the ground multiplet,[17−19]

Received: December 8, 2020
Published: March 8, 2021

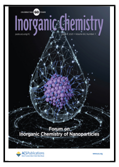

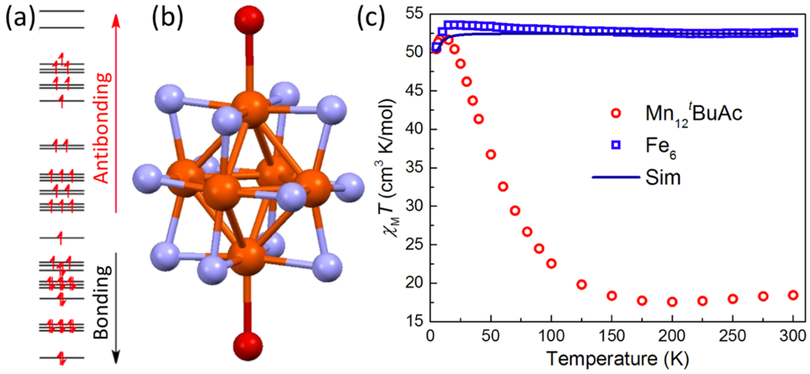

Figure 1. (a) Qualitative energy level diagram representing the single-valence (d-) orbital manifold of states associated with the six metal−metal bonded Fe atoms in the Fe_6 molecule (energy in arbitrary units).[38] These states populate according to Hund's rules, accounting for the $S = {}^{19}/_2$ giant-spin ground state. (b) Ball-and-stick model of the core of the Fe_6 molecule; only the Fe ions (orange) and their first coordination shell, including N (light blue) and O (red) atoms, are shown. (c) Comparison of DC $\chi_M T$ ($\propto \mu_{\mathrm{eff}}^2$, where μ_{eff} is the effective molecular magnetic moment) versus T results for Fe_6 and $Mn_{12}{}^t$BuAc (from ref 45), both measured at 0.1 T; a simulation of the Fe_6 result employing the ZFS parameters deduced from this study (see Table 1) is given by the solid line. As can be seen, the effective giant magnetic moment of the Fe_6 molecule persists to room temperature, whereas that of the Mn_{12} molecule drops precipitously starting at ∼10 K. By 100 K, the spins associated with the Mn_{12} molecule are mostly uncoupled while those of the Fe_6 molecule remain strongly coupled even at room temperature.

which can result in considerable quantum mechanical mixing between ground and excited spin states.[15,20] This mixing is detrimental to both classical information storage and QIP, as it promotes unwanted channels that mediate quantum tunneling of magnetization (QTM)[20−24] and quantum information leakage (loss of fidelity).[25]

To overcome the aforementioned limitations, two new approaches to the development of SMMs with increased blocking temperatures are currently under intense investigation. The first involves the study of individual ions with orbitally degenerate ground states such that their spin and orbital moments are strongly coupled; these include transition metals in certain high-symmetry coordination environments[26−28] and heavier lanthanides.[29−31] This approach has seen an increase in the record blocking temperature from just 4 K for Mn_{12}-acetate[10] to ∼80 K for dysprosocenium,[30,31] a relatively simple mononuclear Dy^{III} sandwich compound. Stabilizing the required giant magnetic anisotropy in a single ion is synthetically challenging, usually resulting in highly reactive complexes. There is also a fundamental limit to the anisotropy that can be achieved in such mononuclear species, set either by the electrostatic crystal-field interaction between the 4f electron density and the associated ligand set in the case of the lanthanides,[32] or the spin−orbit coupling energy scale in the case of lighter transition metals.[27,28] Meanwhile, it is particularly hard to shut down spin−lattice interactions in monometallic systems. Consequently, efficient magnetization relaxation pathways are inevitable at elevated temperatures, and these ultimately limit T_B.[30,33,34] It is, therefore, advantageous to consider a second approach involving the exploration of novel mechanisms for achieving strong ferromagnetic spin−spin (exchange) interactions between multiple anisotropic metal centers. This is challenging for lanthanides because of the contracted nature of their 4f orbitals, although some successes have been achieved in dinuclear systems with spin-bearing (radical) linkers, e.g., N_2^{3-} radical-bridged dilanthanide complexes,[4] as well as the endohedral metallofullerenes $Ln_2@C_{80}(CH_2Ph)$[3] and $Ln_2@C_{79}N$ (Ln = Dy, Tb).[35,36] Unfortunately, one again finds that there is a fundamental limitation in such situations that is set by the maximum achievable exchange interaction strength.[4] Consequently, one inevitably comes back to exploring innovative solutions to the problem of achieving strong magnetic exchange within multinuclear SMMs. Of particular interest in this regard is the possibility of linking spin centers via direct metal−metal bonds,[37−40] the main topic of this article.

In metal−metal bonded systems, one can no longer describe the magnetism in terms of the assembly of discrete ions with well-defined (trapped) valence states and associated magnetic moments. Instead, one must consider a single molecular orbital manifold, occupied by the sum total of the valence electrons involved in bonding (see Figure 1a).[38] Achieving a giant-spin ground state in such systems still represents a formidable challenge. Strong metal−metal bonds give rise to molecular-orbital splittings that typically exceed the spin-pairing energy, resulting in low-spin configurations ($S = 0$ or ${}^1/_2$).[40] Therefore, an intermediate regime is desirable, involving relatively weak metal−metal bonds, such that the orbital energies favor single (Hund's rule) occupancy.[38,41] However, the metal−metal interactions should nevertheless be sufficiently strong to ensure sufficient isolation of the ground state from excited orbital/spin states.

Recently, the compound $[Bu_4N][({}^HL)_2Fe_6(solv)_2]$ was synthesized, where solv = dmf (*N*,*N*-dimethylformamide) or py (pyridine), and ${}^HLH_6 = MeC(CH_2NHPh\text{-}o\text{-}NH_2)_3$;[37,38] only the dmf version (hereon Fe_6, see Figure 1b) was studied in the present work. The Fe_6 molecule is characterized by relatively short Fe···Fe distances ($d_{\mathrm{Fe-Fe}} \approx 2.65$ Å) associated with the desired metal−metal bonding. Magnetic measurements indicate a ground state spin of $S = {}^{19}/_2$, with no measurable population of excited spin states up to at least room temperature (Figure 1c).[38] Furthermore, slow magnetization relaxation is observed below 5 K. Thus, Fe_6 represents one of the first truly molecular examples of a metal−metal-bonded superparamagnet[10] (a SMM). However, a thorough spectroscopic investigation of this molecule has so far been lacking.

We report here a comprehensive study of the Fe_6 molecule using a variety of state-of-the-art high-frequency magnetic resonance techniques. At the same time, we make detailed comparisons with the original polynuclear SMM, Mn_{12},[42,43] which is similar in many respects to Fe_6 except for the nature of the exchange interactions coupling the spins, giving rise to giant-spin ground states. For example, the magnetic moments associated with these states differ only in a single unpaired electron, i.e., $\sim 19\mu_B$ ($S = {}^{19}/_2$) versus $\sim 20\mu_B$ ($S = 10$) for Fe_6 and neutral Mn_{12}, respectively. Meanwhile, both molecules possess very similar axial magnetic anisotropy energy scales, as quantified by their so-called electron paramagnetic resonance (EPR) magnetization relaxation barriers, U_{EPR}, which measure the theoretical energy difference between the lowest and highest-lying M_S states on the basis of a purely axial ZFS parameterization, i.e., ignoring axial symmetry breaking: $U_{EPR} = 45.6$ cm^{-1} ($\approx |D|S^2$, with $D = -0.507(2)$ cm^{-1}, vide infra) for Fe_6 and ~ 47 cm^{-1} [$D = -0.463(4)$ cm^{-1}, plus a significant 4th-order contribution] for Mn_{12}.[44] The one obvious difference, however, is the isolated nature of the spin ground state for Fe_6 compared to Mn_{12}. This is illustrated in Figure 1c, which compares the temperature dependences of the effective moments (proportional to the molar magnetic susceptibility-temperature product, $\chi_M T$). While Fe_6 maintains $\chi_M T \approx 50$ cm^3·K·mol^{-1} expected for a $S = {}^{19}/_2$ ground state (with $g \approx 2$) all the way to room temperature,[38] the value for Mn_{12} drops precipitously from a maximum close to that expected for $S = 10$ (55 cm^3·K·mol^{-1}) at $T = 10$ K, to below 20 cm^3·K·mol^{-1} at 100 K,[45] indicating partially uncoupled spins, i.e., the population of low-lying spin states. In the absence of a microscopic electronic description of the Fe_6 molecule, we turn to spectroscopic measurements to provide further insights into the isolated nature of its $S = {}^{19}/_2$ ground state. The reported measurements support the findings of the magnetic data (Figure 1c), whilst also adding weight to previous theoretical work noting the connection between spin state mixing and a breakdown of the giant-spin approximation.[20−24]

METHODS

Frequency-domain Fourier-transform (FD-FT) terahertz (THz) EPR experiments were performed using the THz beamline of the BESSY II synchrotron at the Helmholtz-Zentrum Berlin.[46−48] Coherent synchrotron radiation emitted in the low-α operation mode[49] is first passed through a Fourier-transform infrared spectrometer (Bruker IFS 125 HR) with a frequency resolution set to 6 GHz (the maximum resolution is 190 MHz). Elliptical mirrors then focus the THz beam onto the sample, which was placed in the variable-temperature insert of an optical superconducting magnet (Oxford Spectromag 4000, with a maximum field of ±10 T in normal operation and ±11 T under pumped liquid helium conditions). The transmitted signal is detected by a Si bolometer cooled to 1.6 K and, finally, the absorbance is evaluated according to the procedure described in the Supporting Information (Figure S1). The polycrystalline samples used for the FD-FT experiments were each mixed with ~100 mg of polyethylene and pressed into pellets. The properties of the three samples were found to be essentially identical and, because of the limited access to the spectrometer, only one was studied in detail.

Field-swept high-field EPR (HFEPR) experiments were performed at multiple fixed frequencies on microcrystalline powder samples at the electron magnetic resonance facility of the US National High Magnetic Field Laboratory (NHMFL) in Tallahassee, Florida.[13] For these purposes, a home-built transmission-type spectrometer was used.[50] Microwave (MW) radiation was generated via a phase-locked source (Virginia Diodes Inc.) with a tunable base frequency of 13 ± 1 GHz. After passing through a variable-frequency multiplier chain (resulting in adjustable frequencies between ~50 and 620 GHz), the radiation propagates through cylindrical light pipes to the sample, placed at the field center of a 15/17 T superconducting magnet (Oxford Instruments Ltd, UK). The transmitted signal is then detected by a fast InSb bolometer (QMC Instruments, UK), which permits the use of field modulation (at up to 50 kHz) and lock-in detection at the first harmonic. Consequently, the powder HFEPR spectra are recorded as a derivative, dI/dB_0, where I is the transmitted MW intensity, then plotted versus the applied magnetic field, B_0. Carefully ground powder samples of Fe_6 (~50 mg) were loaded into polyethylene sample cups. In total, three samples were prepared and investigated separately. All three were found to give essentially identical results and, therefore, only one of them will be discussed here. The sample temperature was varied between ~8 K and room temperature using a continuous-flow cryostat (Oxford Instruments Ltd, UK).

Angle-dependent HFEPR measurements were also performed on a single crystal using a cavity perturbation technique. For these purposes, a millimeter-wave vector network analyzer (AB Millimetre, France) was employed as both a MW source and phase-sensitive detector.[51,52] Spectra were recorded at the fixed frequency of 263.7 GHz in a 9−5 T superconducting vector magnet (Cryogenics Ltd, UK, with 9 T vertical and 5 T horizontal fields)[53] with a variable-flow He gas cryostat used to stabilize the sample temperature at 1.8 K. A single crystal was mounted on the base plate of a vertical overmoded cylindrical resonator. The orientation of the static applied magnetic field, B_0, is described by polar and azimuthal angles θ and ϕ, respectively: θ was varied relative to the vertical cylindrical axis of the resonator in 10° increments using the 9 and 5 T coils of the vector magnet (maximum vector field is 4.5 T); meanwhile, ϕ was varied in 10° increments by physically rotating the resonator about the vertical axis. As such, these coordinates are referenced to fixed axes associated with the resonator and bear no direct relation to the crystallographic axes; attempts to relate the two were ultimately unsuccessful due to the low symmetry space group ($C2/c$) and irregular crystal shape.

Kohn−Sham density functional theory (DFT) calculations were carried out with Turbomole 6.5[54] employing the B3LYP exchange−correlation functional[55,56] in combination with Ahlrichs' def2-TZVP basis set,[57] as single-point calculations on the X-ray crystallographic molecular structure (with the positively charged counterion not considered). The convergence criterion for the total energy in the self-consistent field algorithm was set to 10^{-7} hartree. The spin density was plotted with UCSF Chimera 1.14.[58]

For this investigation, crystals of $[Bu_4N][(^{H}L)_2Fe_6(dmf)_2]$ were synthesized according to the procedure described in ref 38. All sample manipulations were carried out under argon or nitrogen atmospheres. When outside of a glovebox, samples were kept at liquid-nitrogen temperatures and rapidly loaded cold into the various spectrometers. Simulations of magnetic and spectroscopic data were based on the spin Hamiltonian formalism (see eq 1 below) and were performed using EasySpin (version 5.2).[59−61]

HIGH-FREQUENCY EPR STUDIES OF Fe_6

The magnetic and spectroscopic properties of a well-isolated, giant-spin ground state can be described using the following spin Hamiltonian[10,23]

$$\hat{H} = D\left[\hat{S}_z^2 - {}^1/_3 S(S+1)\right] + E(\hat{S}_x^2 - \hat{S}_y^2) + \sum_{k=4,6..}\sum_{q=-k}^{k} B_k^q \hat{O}_k^q + \mu_B \mathbf{B}_0\cdot\mathbf{g}\cdot\hat{\mathbf{S}} \qquad (1)$$

The first two terms describe the axial and rhombic 2nd-order ZFS interactions, parameterized by D and E, respectively ($\hat{S}_i$ are spin component operators, with $i = x, y, z$); the coordinate system is molecule-fixed and chosen such that $0 \leq |E/D| \leq {}^1/_3$, with the z-axis defined along the dominant anisotropy direction. The third term acknowledges the fact that it is sometimes necessary to include 4th- and higher-order ZFS terms to obtain a satisfactory description of spectroscopic data, particularly as the giant-spin approximation begins to break down because of the existence of low-lying excited spin multiplets;[20,24] $\hat{O}_k^q$ represent conventional extended Stevens operators (ESOs − polynomials in $\hat{S}_i$) of rank k, with q specifying the rotational symmetry, parameterized by the associated B_k^q coefficients.[62] Of particular relevance in this work is the 4th-order axial term ($k = 4$, $q = 0$) with operator

$$\hat{O}_4^0 = 35\hat{S}_z^4 - (30\mathbb{s} - 25)\hat{S}_z^2 + (3\mathbb{s}^2 - 6\mathbb{s}) \quad (2)$$

where $\mathbb{s} = S(S + 1)$. The last term in eq 1 describes the Zeeman interaction with the external magnetic field, $\mathbf{B}_0$, where $\mathbf{g}$ denotes the g-tensor, assumed to be diagonal, μ_B denotes the Bohr magneton, and $\hat{\mathbf{S}}$ the total spin operator. The sign of D determines the nature of the anisotropy, either easy-plane ($D > 0$) or easy-axis ($D < 0$).[10] The latter results in an energy barrier separating the two M_S states with maximal spin projection ($M_S = \pm S$). This barrier is the primary contributor to the slow magnetization relaxation in polynuclear SMMs.[42,43] The accurate spectroscopic determination of this barrier requires radiation with energy comparable to that of the separation between the lowest-lying (i.e., thermally populated) M_S states. For most SMMs ($D < 0$), this gap is of order $(2S - 1)|D|$, or $18|D|$ for Fe_6, and can range from a few GHz to several THz. Therefore, broadband approaches such as multifrequency HFEPR and FD-FT THz EPR are required to directly determine the ZFS parameters in eq 1.[13,63]

Powder Measurements. *FD-FT THz EPR.* In frequency-domain EPR, the MW frequency is swept while the magnetic field remains fixed. The advantage of this technique is that it allows for the direct observation of zero-field transition frequencies/energies in the absence of an applied magnetic field. This approach has proven successful for the determination of ZFS in both coordination compounds and metalloproteins.[46,64] The FD-FT THz EPR absorbance spectra of an Fe_6 powder are shown together with simulations in Figure 2. In zero applied field and at the base temperature of the variable-temperature insert (5 K), a single symmetric absorption feature (resonance) is clearly observed above the noise at 264 GHz. Simulations of the field-dependent spectra employing the spin Hamiltonian parameters obtained from the combined FD-FT THz EPR and field-swept HFEPR studies (vide infra) reproduce the trends seen in the data: the spectral weight associated with the 264 GHz resonance spreads out upon application of the field because of the anisotropic nature of the ZFS tensor; this reduces the overall intensity of the resonance, making it hard to discern above the noise for fields greater than 2 T. Nevertheless, the strong zero-field peak can clearly be assigned as a magnetic−dipole transition on the basis of its field dependence. Variable-temperature measurements (Figure S1, Supporting Information) indicate that the signal intensity associated with this peak decreases with increasing temperature. Therefore, on the basis of the anticipated negative D parameter, we assign this resonance to the transition between the $M_S = \pm^{19}/_2$ and $\pm^{17}/_2$ ground and first excited Kramers doublets (corresponding to z_1 in Figures 3−5). One can then make an initial estimate of $D \approx (-264\text{ GHz})/18 \cong -0.49\text{ cm}^{-1}$.

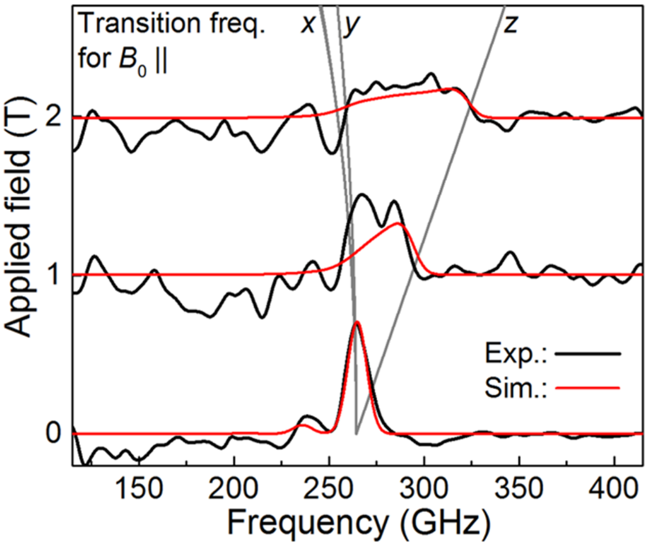

Figure 2. FD-FT THz EPR absorbance spectra recorded at 5 K for a pressed polyethylene/Fe_6 powder pellet, offset according to the field at which they were measured and proportionally rescaled to arbitrary units on the ordinate. Black lines represent the experimental spectra and the red lines are simulations performed with the optimum ZFS parameterization (vide infra). The labeled gray lines depict transition frequencies as a function of the magnetic field, B_0, applied parallel to the x-, y-, and z-axes defined by the ZFS tensor.

Field-Swept HFEPR. Experimental spectra obtained for a powder Fe_6 sample, recorded at ~8 K and various frequencies

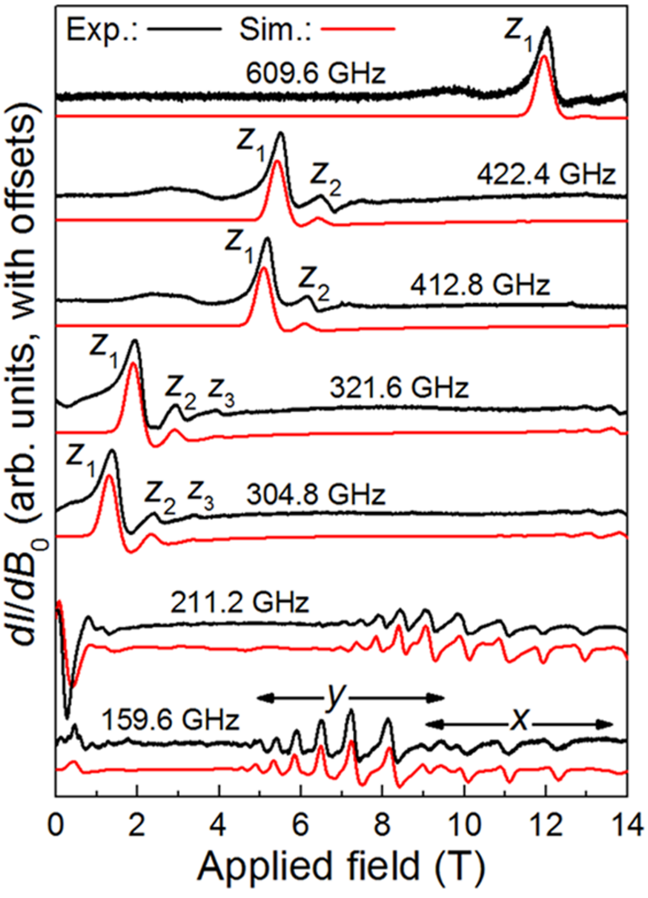

Figure 3. Multifrequency HFEPR spectra for a powder sample of Fe_6. All measurements were made at a temperature of ~8 K and at the indicated frequencies. Spectra are offset and rescaled for clarity. Black lines are the experimental data, while red lines correspond to simulations assuming a giant-spin $S = {}^{19}/_2$ state with the parameters given in Table 1. Several of the resonances have been labeled, as discussed in the main text; x, y, and z denote regions of the spectra associated with crystallites that have the magnetic field aligned with the corresponding axes of the ZFS tensor.

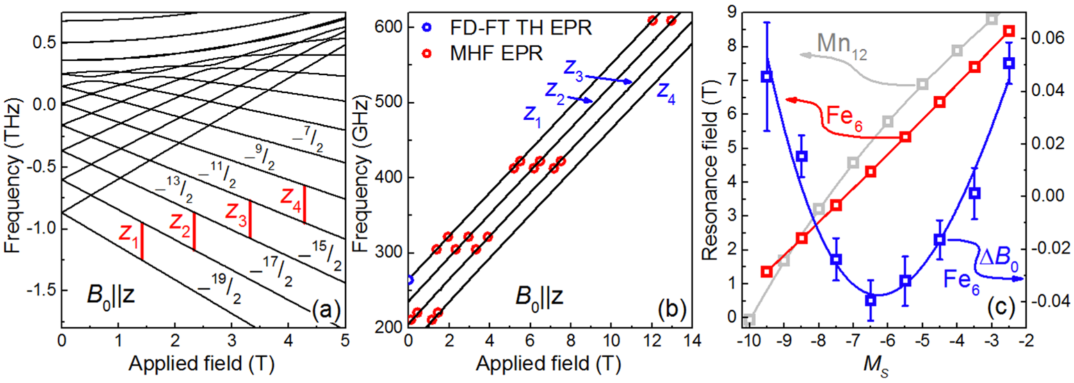

Figure 4. (a) Zeeman energy level diagram for Fe_6 as a function of magnetic field applied parallel to the z-axis of the ZFS tensor, assuming the parameters given in Table 1; the lowest lying levels are labeled according to the associated (approximate) spin projection, M_S. The first four easy-axis ($B_0||z$) transitions labeled z_1 to z_4 are indicated by the vertical red bars corresponding to a frequency of 304.8 GHz. (b) Experimental peak positions corresponding to resonances z_1 to z_4 deduced from the HFEPR measurements in Figure 3 (red circles) and the lone 264 GHz data point at zero field (blue circle) deduced from the FD-FT THz EPR spectra (Figure 2). Solid lines are simulations based on the parameters given in Table 1. (c) Plot of 304.8 GHz resonance position (referenced to the left axis) versus the spin projection, M_S, associated with the state from which the transition was excited for both Fe_6 (in red) and $Mn_{12}BrAc$ (in gray); the Fe_6 data points were deduced from measurements at multiple temperatures (Figure 5), while the points for Mn_{12} were generated at the same frequency using the ZFS parameters reported in ref 44. A clear curvature is seen for Mn_{12}, while a curvature of opposite sign is only observable for Fe_6 after subtracting a linear regression, resulting in the deviation from linearity, ΔB_0 (in blue), referenced to the right axis.

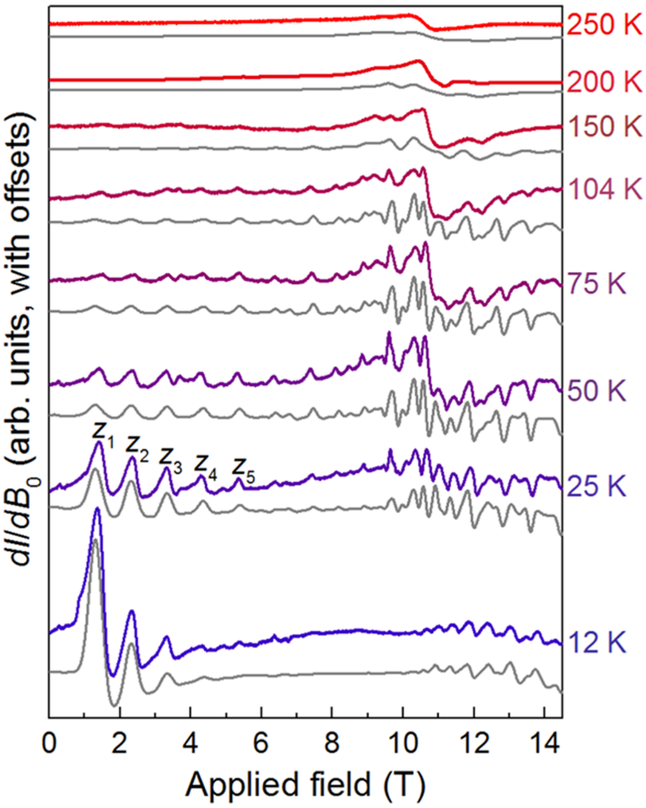

Figure 5. HFEPR spectra of Fe_6, measured at 304.8 GHz and at the temperatures indicated on the right. Thick lines (color indicates temperature, from blue for low toward red for high) are the experimental spectra. Simulations according to eq 1 employing the parameters in Table 1 are shown as gray lines below each experimental spectrum. Several of the easy-axis resonances are labeled above the 25 K spectrum.

in the range from 160 to 610 GHz, are shown in Figure 3. Superimposed below each spectrum is a simulation generated using the optimum ZFS parameterization (vide infra). Resonance positions deduced from turning points in the powder EPR spectra for crystallites with $B_0||z$ are plotted versus frequency in Figure 4b. The strongest of these (the peak labeled z_1 in Figure 3) lies on a straight line with a zero-field intercept at 264 GHz, in perfect agreement with the zero-field gap determined from the FD-FT THz EPR measurements. Careful inspection of the HFEPR spectra recorded above ~200 GHz reveals a series of peaks that decrease in intensity as the field strength increases (labeled z_1–z_4 in Figures 3–5). The decreasing intensity pattern coupled with the linear response to magnetic field [with average slope corresponding to g_z = 2.05(1)] confirms that this series of transitions arises from a system with $D < 0$ and the z-axis of the anisotropy tensor parallel to the external magnetic field.

In the simplest parametrization scheme, i.e., one that considers only 2nd-order axial ZFS (the first term in eq 1), the zero-field transition energy of z_1 ($M_S = -^{19}/_2 \rightarrow -^{17}/_2$) is given by $18|D|$. The next transition energy (z_2: $M_S = -^{17}/_2 \rightarrow -^{15}/_2$) is then reduced by $2|D|$ relative to z_1, i.e., $16|D|$. This pattern continues for the subsequent Kramers pairs, resulting in an exactly linear relationship between transition energy, $\delta\varepsilon(M_S)$, and the spin projection, M_S, associated with the state from which the transition was excited ($M_S = -^{19}/_2$ for z_1, etc.). This simple relationship arises because the first term in eq 1 gives rise to eigenvalues that are quadratic in M_S, i.e., $\varepsilon(M_S) \propto DM_S^2$, whereas EPR measures energy differences, $\delta\varepsilon(M_S) \propto 2DM_S$; hence, the slope associated with a plot of δ_ε versus M_S is constant, $\delta^2\varepsilon/\delta M_S^2 = 2D$. In a fixed-frequency field-swept experiment, a higher resonance field corresponds to a smaller transition energy (Figure 4a) and, because the Zeeman interaction is linear in the field for $B_0||z$, a plot of resonance field versus M_S should also be exactly linear, i.e., the D-only parameterization should lead to equal spacing between the $B_0||z$ resonances. On the basis of the four lines corresponding to resonances z_1 to z_4 at 8 K in Figure 4b, it is hard to visually discern any deviation from such an equal spacing. We, therefore, performed variable-temperature measurements (Figure 5) at a frequency of 304.8 GHz in order to thermally populate higher-lying M_S levels and, therefore, evaluate the positions of more $B_0||z$ resonances. The average positions of eight such transitions, deduced from spectra recorded at multiple temperatures, are plotted versus M_S in Figure 4c. Visual inspection again seems to indicate that the red data points lie on a perfectly straight line (equal spacing), suggesting a *D*-only parameterization. This important observation is in stark contrast to well-known superexchange-coupled SMMs such as Mn_{12}, where the spacing between $B_0 \| z$ resonances varies significantly with M_S, an effect that requires introduction of a significant 4th-order axial ZFS interaction. In fact, the positions of the first eight 304.8 GHz resonances for Mn_{12}BrAc fall in essentially the same magnetic-field range,[65,66] and are included in Figure 4c for comparison (gray squares), where a very significant curvature can be seen when compared to the Fe_6 data.

Subtraction of a linear regression from the Fe_6 data does in fact reveal a weak nonlinear behavior (blue data points plotted in Figure 4c as the deviation from linearity, ΔB_0, against the scale on the right-hand axis) that is not discernible visually, although it clearly exceeds the error bars on the data. The curvature is of opposite sign to Mn_{12},[44] and its amplitude over the eight resonances is about an order of magnitude weaker than seen for Mn_{12}. A fit to a cubic polynomial is superimposed on the ΔB_0 data, enabling estimation of the $\hat{S}_z^4$ coefficient ($= 35B_4^0$) in eq 1 upon adding the axial 4th-order term given in eq 2; note that any $\hat{S}_z^2$ dependence has been removed entirely via subtraction of the linear regression, leaving behind only a cubic dependence of $\delta\varepsilon$ on M_S (it is cubic in response to the $\hat{S}_z^4$ operator in the same way that the 2nd-order dependence is linear in response to $\hat{S}_z^2$, as discussed above). From this analysis, one can obtain an initial estimate of $B_4^0 \approx +2.8 \times 10^{-6}$ cm^{-1}. As discussed below, the possible existence of a rhombic anisotropy (*E* term in eq 1) for Fe_6 complicates this analysis somewhat, as it also contributes to a very weak nonlinearity of the $B_0 \| z$ resonance positions plotted in Figure 4c, though the effect is almost an order of magnitude weaker. Nevertheless, this means that there is an interdependence between *E* and B_4^0 in the fit to the data in Figure 4c. Hence, the optimum value of $B_4^0 = +2.3(3) \times 10^{-6}$ cm^{-1} for Fe_6 was deduced from combined simulations of the entire powder EPR data set (vide infra). For comparison, an order of magnitude larger value of $B_4^0 = -2.5(3) \times 10^{-5}$ cm^{-1} has been reported for Mn_{12}BrAc,[44,65,66] providing the first quantitative spectroscopic evidence for the isolation of the $S = {}^{19}/_{2}$ ground state in Fe_6 relative to well-known superexchange-coupled SMMs, as the sizeable B_4^0 ZFS parameter found for Mn_{12} is known to result from spin-state mixing between the ground term and nearby excited multiplets.[23,67] We comment on this in the following section.

Although an excellent reproduction of the resonance positions corresponding to the low-energy $B_0 \| z$ transitions in Figures 3 and 4 is possible based on a purely axial ZFS parameterization ($E = 0$), the regions of the spectra corresponding to crystallites with $B_0 \| x$ and $B_0 \| y$, particularly those recorded at lower MW frequencies (e.g., 159 GHz in Figure 3), are not well reproduced. This suggests a deviation from axial anisotropy and, therefore, a rhombic *E* term must be included in the spin Hamiltonian, resulting in the $B_0 \| x$ transitions shifting to higher fields while those with $B_0 \| y$ shift to lower fields, with the separation between $B_0 \| x$ and $B_0 \| y$ resonances providing a measure of the magnitude of *E*. Because the transverse Zeeman interaction term $[\mu_B(g_x B_x \hat{S}_x + g_y B_y \hat{S}_y)]$ does not commute with the dominant axial ZFS term, $D\hat{S}_z^2$, the Zeeman splitting for this field orientation is greatly reduced relative to $B_0 \| z$. Consequently, a significant number of states are thermally populated, even at the lowest temperature (8 K) used in our measurements, resulting in many more observed transitions for both $B_0 \| x$ and $B_0 \| y$. We find that there is significant overlap between the spectral components associated with these two orientations (see Figure 3). Therefore, procedures such as those employed above in estimating the axial ZFS parameters are infeasible, not only because of the difficulty of deconvoluting the $B_0 \| x$ and $B_0 \| y$ spectral features, but also because it is not possible to obtain simple analytic expressions for the resonance positions; these are governed by off-diagonal terms in the 20 × 20 spin Hamiltonian matrix for $B_0 \| x$ and $B_0 \| y$, for the 0 to 14 T field range, i.e., the true high-field limit ($g\mu_B B_0 \gg DS$) has not yet been reached. Therefore, simulation of the powder spectra involving matrix diagonalization is necessary. Through simulation of the combined frequency- and temperature-dependent dataset (Figures 3 and 5), we arrive at the self-consistent parameters given in Table 1. This model successfully reproduces both the $S = {}^{19}/_{2}$ powder HFEPR and FD-FT THz EPR experiments as well as the magnetization data (Figure 1).

Table 1. Low-Temperature (<50 K) Spin Hamiltonian Parameters Deduced for Fe_6 from Simulation of the Combined Powder HFEPR Dataset (see eq 1)

parameter	value
D[a]	$-0.507(5)$ cm^{-1}
$\lvert E \rvert$[a]	$0.090(2)$ cm^{-1}
$\lvert E/D \rvert$	$0.180(4)$
Δ_D[b]	0.022 cm^{-1}
Δ_E[b]	4.5×10^{-3} cm^{-1}
B_4^0	$+2.3(3) \times 10^{-6}$ cm^{-1}
g_x	2.04(1)
g_y	2.06(1)
g_z	2.05(1)

[a] Uncertainties refer to the mean values of the associated distributions.
[b] Values correspond to the full widths at half maximum of the distributions ($= 2.35\sigma$, where σ is the standard deviation).

In order to reproduce not only the resonance positions, but also the overall variation in linewidth across the entire HFEPR dataset, it is necessary to include strains (distributions) in the 2nd-order ZFS parameters (gaussian distributions in both *D* and *E* with full widths at half maximum Δ_D and Δ_E, respectively, see Table 1) in addition to an intrinsic peak-to-peak linewidth, $\Delta_{pp} = 125$ mT characteristic of the sharpest features in the low-temperature spectra (see Figure 5). Such strains, which are well documented in other polynuclear SMMs such as Mn_{12},[68−72] arise because of molecule-to-molecule structural variations that modulate the ZFS interactions. They account for the broader resonances at the extremes of the spectra, particularly those for $B_0 \| z$ that are shifted furthest from the isotropic $g \approx 2.05$ position (≈10.6 T in Figure 5), e.g., z_1 is considerably broader than z_5. The simulations were optimized so as to match the intensities of the $B_0 \| z$ resonances, resulting in $B_0 \| x$ and $B_0 \| y$ features that are slightly stronger than those observed experimentally. This suggests a slight ordering of the powder sample favoring the $B_0 \| z$ microcrystals. This effect is well known for highly anisotropic SMMs and was not corrected for in the final simulations as it does not affect the reported parameters.

A remaining curiosity is the persistence of the pronounced inflection in the otherwise flat dI/dB_0 signal seen at the highest temperatures at 10.6 T in Figure 5. Simulations based on the low-temperature parameterization given in Table 1 indicate that it should still be possible to observe a multiline spectrum up to the highest temperatures (assuming the same spectrometer sensitivity), suggesting increased relaxation and dynamics at elevated temperatures, which broaden and wash out the spectrum. Therefore, larger strains were employed in the simulations at temperatures above 50 K, along with a slight increase in the peak-to-peak linewidth: @150 K, Δ_D = 0.03 cm^{-1}, Δ_E = 0.02 cm^{-1}, Δ_{pp} = 250 mT; @ 250 K, Δ_D = 0.13 cm^{-1}, Δ_E = 0.07 cm^{-1}, and Δ_{pp} = 300 mT. Maintaining a relatively small value of Δ_{pp} has the effect of preserving the inflection at the isotropic position (10.6 T in Figure 5), as transitions occurring in this range are insensitive, to first order, to strain. It is also possible that an onset of thermal population of excited spin states accounts for the stronger inflection observed experimentally at 250 K. However, without a multielectron description, there is no way to construct a meaningful model that would capture the population of excited spin states. Assuming the Δ_{pp} = 300 mT linewidth is due to increased relaxation, it corresponds to a lifetime of ~20 ps, which is not unexpected for an anisotropic giant spin with associated spin−lattice coupling; even the most isotropic molecular spins are known to possess sub-μs spin−lattice relaxation times at room temperature,[73] and the corresponding intrawell (not to be confused with overbarrier) relaxation times for anisotropic spins are typically much shorter. Meanwhile, the variation in strain may be attributed to increased disorder at elevated temperatures.

■ ANGLE-DEPENDENT SINGLE-CRYSTAL MEASUREMENTS

To further investigate the Fe$_6$ compound, a series of angle-dependent EPR studies were performed on a single crystal. Unlike the powder HFEPR measurements presented above, the spectra were recorded in transmission mode, hence, resonances are observed as dips in the transmitted intensity, I. The data were collected at low temperature of 1.8 K in order to ensure population of only the lowest spin sublevels, i.e., M_S = $\pm^{19}/_2$ at low field, thereby simplifying the analysis. Angle-dependent spectra obtained at a MW frequency of 263.7 GHz for one plane of rotation (ϕ = 10°) are displayed along with simulations in Figure 6. The first thing to note is that all resonances are observed significantly above zero field. This finding is at odds with the results of the powder measurements, where the ground state transition (z_1) intersects the ordinate at exactly 264 GHz (Figure 4b), and suggests different ZFS parameters for the single crystal employed in these measurements. A detailed characterization of this sample was not feasible because of the limited field range afforded by the vector magnet. However, simulations of the full angle-dependent dataset yield a value for the 2nd-order axial ZFS parameter D = −0.45(1) cm^{-1} (vide infra). This reduction of D by more than 10% compared to the powder sample is not currently understood. The single-crystal measurements were performed subsequent to the powder studies on a newly synthesized batch of samples. One possibility could be the existence of different polymorphs that result from minor variations in crystallization conditions,[74] such that powder and crystal measurements were performed on slightly different structures. Alternatively, it may hint at subtle structural transformations brought about by the grinding of the powder samples.

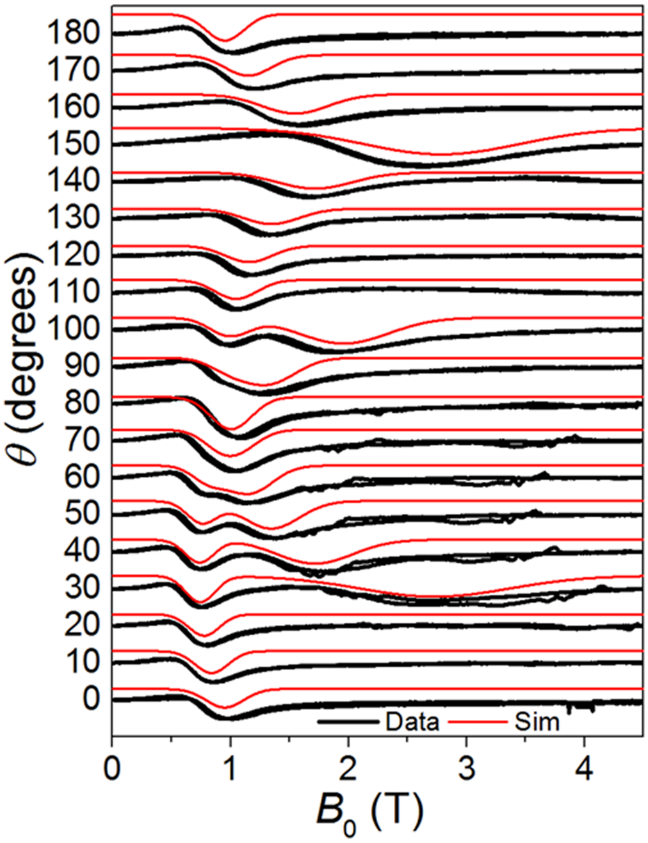

Figure 6. Angle-dependent single-crystal EPR spectra at 10° intervals in the polar angle, θ, from 0 to 180° for the azimuthal ϕ = 10° plane of rotation. Experimental spectra recorded at 263.7 GHz and 1.8 K for both up and down magnetic field sweeps are shown in black; the noise seen in the 1.5 to 4 T range at some of the lower angles is because of a minor mechanical instability in the EPR probe. Simulations are also shown in red above each experimental spectrum, generated assuming the following parameters appropriate to the single crystal: D = −0.45(1) cm^{-1}, g_z = 2.05, and Δ_D = 0.015 cm^{-1}. The MW transmission spectra have been proportionally normalized to arbitrary units and offset according to the value of θ on the ordinate in order to aid viewing; resonances are observed as dips in transmission.

The next thing to note from the low temperature spectra in Figure 6 is the fact that two resonances are observed at most angles, suggesting the presence of two molecular species in the sample. In fact, in the $C2/c$ space group,[38] one does expect spectroscopically distinct sites in the unit cell: four structurally equivalent sites, with pairs related by inversion, resulting in two unique orientations. As such, one may expect superimposed single-crystal EPR spectra for these two molecular orientations, with identical ZFS parameters, albeit differently aligned tensors. For field orientations close to the easy-axis of either species, one expects a relationship between the MW frequency, f, and the resonance position, B_{Ri} (i = 1,2), of the form $f \approx \delta + \gamma B_{Ri}\cos(\psi_i)$, where $\delta = 18|D|/h$ = 243 GHz, $\gamma = g_z\mu_B/h$ = 28.7 GHz/T is the gyromagnetic ratio (assuming the same value for g_z as the powder sample), and ψ_i is the angle between the applied field and the local easy-axis associated with a given species. This expression is approximate in the sense that it considers only the diagonal elements of the spin Hamiltonian matrix of eq. 1, i.e., terms containing $\hat{S}_z$ and $\hat{S}_z^2$, while also ignoring the 4th-order term (eq 2). For relatively small angles, inversion of the above expression gives $B_{Ri} \approx (f - \delta)/\gamma\cos(\psi_i)$, while transformation to the laboratory coordinate frame simply

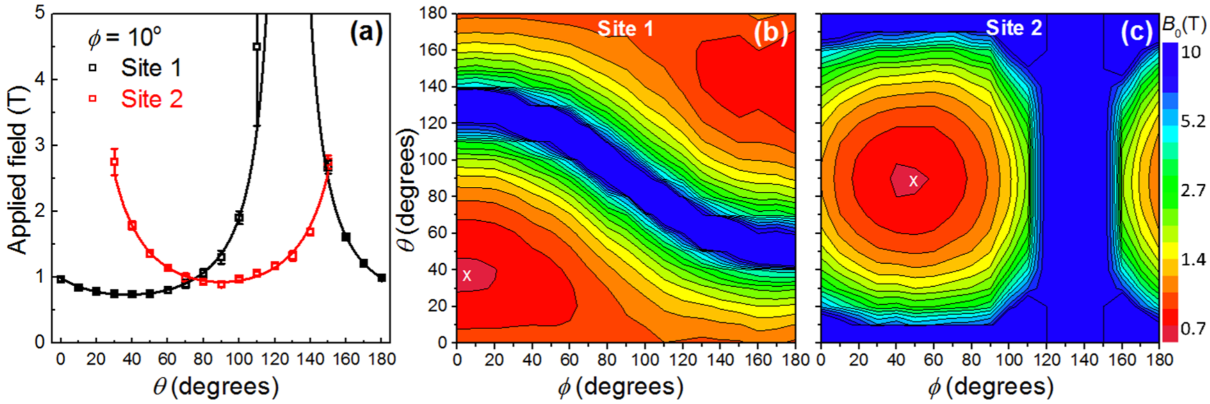

Figure 7. (a) Plot of the 263.7 GHz ground state resonance positions versus polar angle, θ, deduced from the experimental spectra in Figure 6 for the ϕ = 10° plane of rotation. The red and black colors distinguish resonances attributed to the two differently oriented molecular sites within the unit cell. The solid curves are fits to the data for the two sites according to the phenomenological equation given in the main text. (b,c) Two-dimensional false color plots of the resonance positions as a function of θ and ϕ for sites 1 and 2, respectively; the data were generated according to the procedure described in the main text. The white crosses denote the orientations of the magnetic easy (z) axes for each site.

involves replacing cos(ψ_i) by cos($\phi - \phi_i$) cos($\theta - \theta_i$), where θ_i and ϕ_i define the local z axes (in this case, easy axes) of the two molecular orientations. Hence, $B_{\mathrm{R}i}$ is minimum when cos(ψ_i) = 1, i.e., when the applied field is aligned with either of the two z axes. Locating these directions then boils down to repeating the measurements in Figure 6 for multiple planes of rotation and plotting the observed resonance positions (transmission minima) as a function of θ and ϕ over at least a hemisphere; results for ϕ = 10° are displayed in Figure 7a. In order to reduce scatter in the data, resonance positions for each plane of rotation were fit to the phenomenological expression $B_{\mathrm{R}i} \approx A[\cos(\theta - \theta_i)]^{-n}$, where A lumps together the constants, $(f - \delta)/\gamma$, and the unknown cos($\phi - \phi_i$), while the exponent n (generally in the range from 0.6 to 1.0, depending on the range in θ over which resonances are observed) accounts for deviations from the purely axial expression at larger ψ_i. The fits were then used to generate independent two-dimensional false-color plots of $B_{\mathrm{R}i}$ versus θ and ϕ for the two species, as displayed in Figure 7b,c.

Determination of the global minima from the color plots in Figure 7b,c provides the orientations of the z axes associated with the two sites in the crystal structure (white crosses): θ_1 = 37(2)°, ϕ_1 = 5(2)°; θ_2 = 90(2)°, ϕ_2 = 49(2)°. Unfortunately, the irregular shape of the crystal made it impossible to definitively relate these orientations to either the crystallographic or local molecular frames. However, the experimental angular separation of the two local z directions (minor arc of the great circle intersecting these points on the unit sphere), $\Delta\psi^{\mathrm{exp}}$ = 64(3)°, can be compared with the crystal structure by measuring the angle, $\Delta\psi^{\mathrm{cryst}}$, between the differently oriented sites from the vectors formed by the two oxygen atoms in each molecule (see Figure 1). Following this procedure, the tilt angle between the two Fe$_6$ molecules is found to be $\Delta\psi^{\mathrm{cryst}}$ = 61°, in good agreement with the experimentally determined value (to within the estimated uncertainty). Armed with the orientations of the ZFS tensors, it is possible to go back and simulate the angle-dependent EPR transmission curves in Figure 6, with only D and Δ_D as adjustable parameters (taking the value of g_z from the powder measurements and ignoring E). As noted above, an optimum value of $D = -0.45(1)$ cm^{-1} is obtained via this procedure. Meanwhile, the D-strain captures the angle-dependence of the linewidth very well, giving a value that is ~30% smaller (Δ_D = 0.015 cm^{-1}) than found for powders, where identical values (Δ_D = 0.022 cm^{-1}) were obtained for both the FD-FT THz EPR and field-swept HFEPR measurements, suggesting a more ordered structure in the crystal, as would be expected. We note that other widely used EPR spectral broadening mechanisms cannot reproduce the angular variation of the linewidth with just a single parameter.

■ DISCUSSION

Aside from a detailed evaluation of its spin Hamiltonian parameters, the key finding from the previous section concerns the weak 4th-order axial ZFS term for Fe$_6$. In the following discussion, we consider the parameterization given in Table 1 that was deduced from the detailed powder HFEPR measurements. To begin with, it is worth noting that a seemingly miniscule B_4^0 parameter can nevertheless have a pronounced effect on the HFEPR spectra of giant-spin systems, as is the case for Mn$_{12}$, where $B_4^0 \approx -2.5 \times 10^{-5}$ cm^{-1} compares to $D \approx -0.46$ cm^{-1}.[44] The 4th-order axial ESO[62] is given in eq 2, where the sizeable $\hat{S}_z^4$ prefactor and the fact that the expression is quartic (with elements $\propto M_S^4$ and $S^2M_S^2$) means that it can have an outsized influence for giant-spin systems. The leading term, $35\hat{S}_z^4$, which emerges because of mixing of low-lying excited spin states into the ground-state multiplet, makes a very considerable (almost 9 cm^{-1} or ~19%) contribution to the overall anisotropy energy scale, U_{EPR}, for Mn$_{12}$[44] compared to just ~0.8 cm^{-1} (~1.8%) for Fe$_6$. It also results in a spacing between the first two $B_0 \| z$ resonances of almost 2 T for Mn$_{12}$ (Figure 4c), nearly twice that expected on the basis of a D-only parameterization (1.1 T), and twice the spacing found for Fe$_6$. However, this shrinks to <1 T (less even than the spacing for Fe$_6$) for the smallest M_S transitions, which are more-or-less insensitive to the quartic term of the $\hat{O}_4^0$ operator. Only the $\hat{S}_z^4$ interaction within 4th-order ZFS terms can reproduce the highly nonlinear M_S dependence of the $B_0 \| z$ resonance positions seen for Mn$_{12}$ (Figure 4c), which is barely discernible for Fe$_6$. At the same time, only a spectroscopic technique is capable of disentangling these higher-order ZFS interaction terms from the usually dominant 2nd-order terms.[13,43] By contrast, thermodynamic measurements such as DC magnetization or AC susceptibility (excluding QTM spectroscopy)[22] cannot disentangle these effects. As we discuss further below, the 4th-order terms contain important microscopic information and are responsible for the QTM observed in the high-symmetry Mn_{12} SMMs.[15,20−24,75]

From the preceding discussion (and Figure 4c), one gains a clear appreciation for the dramatic impact of the 4th-order ZFS terms in Mn_{12} in comparison to Fe_6. The difference between the two compounds is no surprise when one recognizes that the emergence of effective 4th-order terms is a direct manifestation of microscopic interactions that are not captured in the giant-spin approximation.[15,20] Considering the hypothetical situation of a polynuclear molecule in which the ground-state spin quantum number is exact (i.e., no mixing with excited states that are infinitely far away in energy), one finds that the giant-spin ZFS parameters have an exact correspondence with those associated with the constituent magnetic ions.[76,77] Such a procedure cannot account for the sizeable 4th-order ZFS terms found experimentally for Mn_{12} SMMs.[44] Indeed, related studies of polynuclear systems comprised of $s = 1$ Ni^{II} ions (lowercase s is employed here to differentiate the single-ion properties from those of the coupled system) demonstrate that 4th-order ZFS terms are strictly forbidden on the basis of a simple projection of the single-ion terms onto an exact spin ground state associated with the coupled molecule.[20] This is because the limited 3 × 3 Hilbert space associated with an $s = 1$ object precludes the ZFS terms, $\hat{O}_k^q$, of rank $k > 2$. Nevertheless, sizeable 4th-order molecular ZFS terms are found for polynuclear clusters such as Ni_4, where the individual Ni^{II} ions are weakly coupled via superexchange.[78] Their emergence can be traced to interactions between spin multiplets, i.e., spin state mixing, which perturbs the otherwise pure 2nd-order energy landscape.[20] Spectroscopic characterization of such landscapes then manifest as effective 4th- and higher-order ZFS terms within the giant-spin approximation.

Microscopic models that consider the internal degrees of freedom within polynuclear SMMs demonstrate that the higher-order ZFS terms are related directly to the intrinsic 2nd-order single-ion terms, but that their magnitudes are controlled by the degree of spin state mixing, set by the intramolecular exchange interaction strength, J.[23,24] This, in turn, determines the proximity in energy of excited spin multiplets relative to the ground state. Perturbative analysis shows that the 4th-order terms scale as $\Delta_{SS'}^{-1}$, where $\Delta_{SS'}$ is the energy separation between the states S and S' that are mixed.[24] These energy separations scale with the exchange coupling strength, J, such that $B_4^q \propto J^{-1}$; it can also be shown that $B_6^q \propto J^{-2}$.[15] The same physics holds for Mn_{12}[67] and, even though we do not currently have a microscopic description for Fe_6, one may conjecture that the same idea applies here as well, i.e., the magnitudes of 4th-order ZFS terms should scale with $\Delta_{SS'}^{-1}$. One, therefore, concludes that the order-of-magnitude difference between the B_4^0 parameters deduced for Mn_{12} and Fe_6 implies a similar order-of-magnitude difference in the isolation of their ground states. The first excited $S = 9$ state associated with the Mn_{12}BrAc molecule has been well characterized and determined to be $\Delta_{10,9} \approx 28$ cm^{-1} (40 K) above the $S = 10$ ground state,[18] i.e., the two multiplets overlap significantly. One may then infer that the lowest-lying excited spin states associated with the Fe_6 molecule should be located several hundred wavenumbers (corresponding to several hundred kelvins) above the $S = {}^{19}/_2$ ground state. In other words, the ground state is really well isolated in comparison to Mn_{12}.

The preceding assertion about the isolated nature of the $S = {}^{19}/_2$ ground state of the Fe_6 molecule is borne out by experiment. No evidence is seen in the present EPR studies for the thermal population of anisotropic excited states, i.e., no transitions are seen away from the $g = 2.05$ region that cannot be explained on the basis of an effective $S = {}^{19}/_2$ parameterization; by contrast, such transitions are seen at temperatures as low as 15 K for Mn_{12}BrAc.[18] The only minor deviation from the $S = {}^{19}/_2$ model is the appearance of additional intensity at the isotropic $g = 2.05$ position at elevated temperatures. However, one cannot rule out the possibility that further improvements of the strain modeling could capture this behavior without thermal population of excited states. The susceptibility measurements presented in Figure 1 also support the thermal isolation of the Fe_6 ground state.[38] Although an oversimplification, one can invent a fictitious model based on formal oxidation states, consisting of five Fe^I ($s = {}^3/_2$) and a lone Fe^{II} ($s = 2$), so that one obtains a total spin of $S = {}^{19}/_2$ when the constituent spins couple ferromagnetically. If one then considers a weak coupling limit so that the Fe^I/Fe^{II} spins behave independently at room temperature, one would expect a paramagnetic $\chi_M T$ value of 12.4 cm^3·K·mol^{-1}. This is far below the measured value of 52.6 cm^3·K·mol^{-1} at 300 K (Figure 1).[38] In other words, the magnetic measurements are fully consistent with a well isolated, robust $S = {}^{19}/_2$ ground state (expected $\chi_M T \approx 51$ cm^3·K·mol^{-1}, assuming $g = 2.05$) resulting from the strong ferromagnetic spin−spin interactions within the Fe^6 core. Meanwhile, DFT suggests a delocalized electronic structure having four Fe atoms with 3.5 unpaired electrons each, and two Fe atoms with slightly less than 2 unpaired electrons each, consistent with a mixed-valence situation, and an extra unpaired electron delocalized mostly on the nitrogens (see Figure 8 and Supporting Information). Spectroscopic techniques that allow momentum transfer or spin density

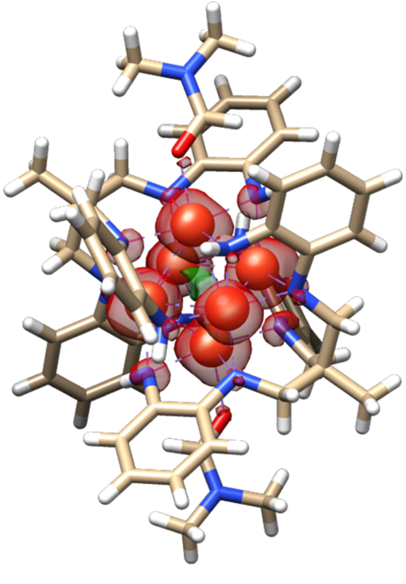

Figure 8. Unpaired spin density from a DFT calculation on the X-ray crystallographic structure of Fe_6 (with the positively charged counterion not considered). Positive (majority) spin density is shaded in red, negative (minority) spin density (only visible at the center of the Fe_6 octahedron) is shaded in green. Fe atoms shown as orange balls, while C, N, O, and H atoms are shown as brown, blue, red, and white edges/ends, respectively. B3LYP/def2-TZVP isosurface value: 0.008 Å^{-3}.

mapping, e.g., neutron scattering,[13] can provide further insights into these issues.

Returning to magnetization dynamics, the relaxation barrier determined from AC susceptibility measurements for Mn_{12} is in good agreement with the value determined from HFEPR. In fact, for reasons discussed in refs 44, 79, it is common for AC measurements to overestimate this barrier. By contrast, the effective barrier to magnetization relaxation determined for Fe_6 from AC measurements, $U_{\mathrm{eff}} = 33.5$ cm^{-1},[38] is significantly lower than the value inferred from the present HFEPR investigation: $U_{\mathrm{EPR}} = 45.7$ cm^{-1} based on a purely axial parameterization, or 51.7 cm^{-1} if the rhombic anisotropy is included. The reason for this reduction in U_{eff} relative to U_{EPR} is because of QTM relaxation, which short-circuits the theoretical maximum (classical) barrier.[80] Although Fe_6 possesses a half-integer spin ground state, meaning that zero-field mixing of degenerate pairs of levels on opposite sides of the barrier is impossible (due to Kramers' theorem), the 6th and 7th doublets, lying, respectively, 34.0 and 37.4 cm^{-1} above the lowest $M_S = \pm^{19}/_2$ ground doublet, split quite rapidly with respect to a transverse field applied in the (hard-) xy plane (tens of MHz in a field of 0.1 mT). Therefore, transverse internal dipolar fields together with the sizeable rhombic ZFS interaction ($|E/D| = 0.18$) likely promote QTM via these levels, thereby explaining the reduction in the effective barrier.

It is interesting to note that the $Fe_6N_{12}O_2$ molecular core (Figure 1) possesses approximate four-fold rotational symmetry. The rhombic ZFS term would be strictly zero for exact four-fold symmetry, meaning that only 4th- and higher-order interactions (i.e., $\hat{O}_k^q$ terms with $k \geq 4$ and $q = \pm 4$) could mediate QTM, as is found for the high-symmetry Mn_{12} variants.[75] Even then, the isolated nature of the ground spin multiplet would ensure that such higher-order interactions are far weaker in the Fe_6 molecule, thus greatly reducing the QTM rate. Crucially, the many-body nature of polymetallic SMMs provides additional protection against QTM relaxation and analogous thermally assisted processes that are known to limit the performance of mononuclear SMMs. Therefore, the possibility of realizing high-symmetry forms of Fe_6 and related metal−metal bonded systems offers exciting prospects in terms of improvements in the performance of polynuclear SMMs, perhaps rivaling or even surpassing the best mononuclear lanthanide SMMs provided the molecular anisotropy can be increased significantly, which remains the primary challenge in cluster-based SMMs. Clearly, an improved fundamental understanding of magnetic anisotropy in metal−metal bonded systems is urgently needed, and a number of such studies are in progress.[40,41]

■ SUMMARY AND CONCLUSIONS

The spin Hamiltonian parameters of an Fe_6 SMM featuring direct metal−metal bonds that give rise to strong ferromagnetic spin−spin interactions and a well-isolated $S = {}^{19}/_2$ giant-spin ground state have been determined precisely via combined FD-FT THz EPR and field-swept HFEPR measurements on both a powder sample and an oriented crystal. The results are contrasted with the well-known and extensively studied $S = 10$ Mn_{12} molecule that features weak intramolecular superexchange interactions and low-lying excited spin states that are detrimental to its SMM properties. In particular, the axial B_4^0 parameter that is a direct consequence of spin-state mixing is an order of magnitude weaker in the Fe_6 molecule, suggesting that the ground state of the molecule is thermally isolated from excited spin states by several hundred wavenumbers. A sizeable 2nd-order rhombic ZFS term is found for the studied Fe_6 molecule, accounting for its relatively low blocking temperature and reduced effective barrier to magnetization relaxation, which is attributed to thermally assisted QTM within the ground $S = {}^{19}/_2$ manifold. In spite of this, the outlook for improving the performance of related metal−metal bonded SMMs is promising, assuming high cluster symmetries can be achieved, which would negate the 2nd-order rhombic ZFS term. Meanwhile, the isolated nature of the spin ground states of such molecules will naturally suppress higher-order interactions capable of mediating QTM.

The high resolution of this combined experimental approach provides excellent constraints on a wide range of spectroscopic parameters, including strains (distributions) in the ZFS parameters that are inferred from variations in EPR linewidths. These, in turn, provide important microscopic details that cannot be inferred from more standard magnetic characterization techniques such as DC and AC susceptometry, including sample preparation-dependent variations in ZFS parameters. Meanwhile, angle-dependent single-crystal HFEPR measurements allow for correlations between magnetic tensors and the underlying crystal structure. Although metal−metal bonded systems have been studied for decades,[81] they have only recently been considered as potential SMMs.[38,39,82,83] The present investigation provides a clear demonstration of the potential of combined wideband EPR methodologies for studies of metal−metal bonded paramagnetic systems, particularly with a view to gaining fundamental microscopic insights that can aid design of future polynuclear SMMs with improved properties.

■ ASSOCIATED CONTENT

Supporting Information

The Supporting Information is available free of charge at https://pubs.acs.org/doi/10.1021/acs.inorgchem.0c03595.

Additional FD-FT THz EPR data and details concerning the DFT calculations (PDF).

■ AUTHOR INFORMATION

Corresponding Authors

Theodore A. Betley − *Department of Chemistry and Chemical Biology, Harvard University, Cambridge, Massachusetts 02138, United States;* orcid.org/0000-0001-5946-9629; Email: betley@chemistry.harvard.edu

Stefan Stoll − *Department of Chemistry, University of Washington, Seattle, Washington 98195, United States;* orcid.org/0000-0003-4255-9550; Email: stst@uw.edu

Stephen Hill − *National High Magnetic Field Laboratory and Department of Physics, Florida State University, Tallahassee, Florida 32310, United States;* orcid.org/0000-0001-6742-3620; Email: shill@magnet.fsu.edu

Authors

Joscha Nehrkorn − *National High Magnetic Field Laboratory, Florida State University, Tallahassee, Florida 32310, United States; Department of Chemistry, Institute for Inorganic and Applied Chemistry, University of Hamburg, 20146 Hamburg, Germany; Department of Chemistry, University of Washington, Seattle, Washington 98195, United States; Max Planck Institute for Chemical Energy Conversion, 45470 Mülheim an der Ruhr, Germany*

Samuel M. Greer − *National High Magnetic Field Laboratory and Department of Chemistry and Biochemistry, Florida State University, Tallahassee, Florida 32310, United States;* orcid.org/0000-0001-8225-3252
Brian J. Malbrecht − *Department of Chemistry and Chemical Biology, Harvard University, Cambridge, Massachusetts 02138, United States*
Kevin J. Anderton − *Department of Chemistry and Chemical Biology, Harvard University, Cambridge, Massachusetts 02138, United States*
Azar Aliabadi − *Berlin Joint EPR Laboratory, Institut für Nanospektroskopie, Helmholtz-Zentrum Berlin für Materialien und Energie, Berlin 12489, Germany*
J. Krzystek − *National High Magnetic Field Laboratory, Florida State University, Tallahassee, Florida 32310, United States;* orcid.org/0000-0001-6088-1936
Alexander Schnegg − *Max Planck Institute for Chemical Energy Conversion, 45470 Mülheim an der Ruhr, Germany; Berlin Joint EPR Laboratory, Institut für Nanospektroskopie, Helmholtz-Zentrum Berlin für Materialien und Energie, Berlin 12489, Germany;* orcid.org/0000-0002-2362-0638
Karsten Holldack − *Institut für Methoden und Instrumentierung der Forschung mit Synchrotronstrahlung, Helmholtz-Zentrum Berlin für Materialen und Energie, Berlin 12489, Germany*
Carmen Herrmann − *Department of Chemistry, Institute for Inorganic and Applied Chemistry, University of Hamburg, 20146 Hamburg, Germany;* orcid.org/0000-0002-9496-0664

Complete contact information is available at:
https://pubs.acs.org/10.1021/acs.inorgchem.0c03595

Notes

The authors declare no competing financial interest.

■ ACKNOWLEDGMENTS

We thank Xenia Engelmann (Humboldt Universität Berlin) for sample preparation for the FD-FT THz-EPR experiments. We also thank G. Christou and C. Lampropoulos for providing the $\chi_M T$ versus T data for $Mn_{12}{}^t$BuAc in Figure 1c. J.N. thanks the Deutsche Forschungsgemeinschaft (DFG) for a Research Fellowship (grant no. NE 2064/1-1). S.M.G. and B.M., respectively, acknowledge support from the National Science Foundation (NSF DGE-1449440) and NSERC for graduate research fellowships. Work performed at the US National High Magnetic Field Laboratory is supported by the NSF (DMR-1644779) and the State of Florida. Additional support from the NSF (DMR-2004732 to S.H. and CHE-1452967 to S.S.) and the Department of Energy, Basic Energy Sciences (DE-SC0008313 to T.A.B.) is also gratefully acknowledged.

■ REFERENCES

(1) Baniodeh, A.; Magnani, N.; Lan, Y.; Buth, G.; Anson, C. E.; Richter, J.; Affronte, M.; Schnack, J.; Powell, A. K. High spin cycles: topping the spin record for a single molecule verging on quantum criticality. *npj Quantum Mater.* **2018**, *3*, 10.

(2) Meihaus, K. R.; Fieser, M. E.; Corbey, J. F.; Evans, W. J.; Long, J. R. Record High Single-Ion Magnetic Moments Through $4f^n5d^1$ Electron Configurations in the Divalent Lanthanide Complexes $[(C_5H_4SiMe_3)_3Ln]^-$. *J. Am. Chem. Soc.* **2015**, *137*, 9855−9860.

(3) Liu, F.; Krylov, D. S.; Spree, L.; Avdoshenko, S. M.; Samoylova, N. A.; Rosenkranz, M.; Kostanyan, A.; Greber, T.; Wolter, A. U. B.; Büchner, B.; Popov, A. A. Single molecule magnet with an unpaired electron trapped between two lanthanide ions inside a fullerene. *Nat. Commun.* **2017**, *8*, 16098.

(4) Demir, S.; Gonzalez, M. I.; Darago, L. E.; Evans, W. J.; Long, J. R. Giant coercivity and high magnetic blocking temperatures for N_2^{3-} radical-bridged dilanthanide complexes upon ligand dissociation. *Nat. Commun.* **2017**, *8*, 2144.

(5) Evangelisti, M.; Candini, A.; Affronte, M.; Pasca, E.; de Jongh, L. J.; Scott, R. T. W.; Brechin, E. K. Magnetocaloric Effect in Spin-Degenerated Molecular Nanomagnets. *Phys. Rev. B: Condens. Matter Mater. Phys.* **2009**, *79*, 104414.

(6) Leuenberger, M. N.; Loss, D. Quantum Computing in Molecular Magnets. *Nature* **2001**, *410*, 789−793.

(7) Gaita-Ariño, A.; Luis, F.; Hill, S.; Coronado, E. Molecular spins for quantum computation. *Nat. Chem.* **2019**, *11*, 301−309.

(8) Hussain, R.; Allodi, G.; Chiesa, A.; Garlatti, E.; Mitcov, D.; Konstantatos, A.; Pedersen, K. S.; De Renzi, R.; Piligkos, S.; Carretta, S. Coherent Manipulation of a Molecular Ln-Based Nuclear Qudit Coupled to an Electron Qubit. *J. Am. Chem. Soc.* **2018**, *140*, 9814−9818.

(9) Chiesa, A.; Macaluso, E.; Petiziol, F.; Wimberger, S.; Santini, P.; Carretta, S. Molecular Nanomagnets as Qubits with Embedded Quantum-Error Correction. *J. Phys. Chem. Lett.* **2020**, *11*, 8610−8615.

(10) Gatteschi, D.; Sessoli, R.; Villain, J. *Molecular Nanomagnets*; Oxford University Press: Oxford, 2007.

(11) Christou, G.; Gatteschi, D.; Hendrickson, D. N.; Sessoli, R. Single-Molecule Magnets. *MRS Bull.* **2000**, *25*, 66−71.

(12) Mannini, M.; Pineider, F.; Sainctavit, P.; Danieli, C.; Otero, E.; Sciancalepore, C.; Talarico, A. M.; Arrio, M.-A.; Cornia, A.; Gatteschi, D.; Sessoli, R. Magnetic Memory of a Single-Molecule Quantum Magnet Wired to a Gold Surface. *Nat. Mater.* **2009**, *8*, 194−197.

(13) Baker, M. L.; Blundell, S. J.; Domingo, N.; Hill, S. Spectroscopy Methods for Molecular Nanomagnets. *Molecular Nanomagnets and Related Phenomena*; Structure and Bonding; Springer, 2015; Vol. *164*, pp 231−292.

(14) Pinkowicz, D.; Southerland, H. I.; Avendaño, C.; Prosvirin, A.; Sanders, C.; Wernsdorfer, W.; Pedersen, K. S.; Dreiser, J.; Clérac, R.; Nehrkorn, J.; Simeoni, G. G.; Schnegg, A.; Holldack, K.; Dunbar, K. R. Cyanide Single-Molecule Magnets Exhibiting Solvent Dependent Reversible "On" and "Off" Exchange Bias Behavior. *J. Am. Chem. Soc.* **2015**, *137*, 14406−14422.

(15) Hill, S.; Datta, S.; Liu, J.; Inglis, R.; Milios, C. J.; Feng, P. L.; Henderson, J. J.; del Barco, E.; Brechin, E. K.; Hendrickson, D. N. Magnetic quantum tunneling: Insights from simple molecule-based magnets. *Dalton Trans.* **2010**, *39*, 4693−4707.

(16) Kahn, O. *Molecular Magnetism*; VCH-Verlag: Weinheim, New York, 1993.

(17) Zipse, D.; North, J. M.; Dalal, N. S.; Hill, S.; Edwards, R. S. Characterization of the $S = 9$ excited state in Fe_8Br_8 by electron paramagnetic resonance. *Phys. Rev. B: Condens. Matter Mater. Phys.* **2003**, *68*, 184408.

(18) Petukhov, K.; Hill, S.; Chakov, N. E.; Abboud, K. A.; Christou, G. Evidence for the $S = 9$ excited state in Mn_{12}-bromoacetate measured by electron paramagnetic resonance. *Phys. Rev. B: Condens. Matter Mater. Phys.* **2004**, *70*, 054426.

(19) Feng, P. L.; Koo, C.; Henderson, J. J.; Manning, P.; Nakano, M.; del Barco, E.; Hill, S.; Hendrickson, D. N. Nanomodulation of Molecular Nanomagnets. *Inorg. Chem.* **2009**, *48*, 3480−3492.

(20) Wilson, A.; Lawrence, J.; Yang, E.-C.; Nakano, M.; Hendrickson, D. N.; Hill, S. Magnetization tunneling in high-symmetry single-molecule magnets: Limitations of the giant spin approximation. *Phys. Rev. B: Condens. Matter Mater. Phys.* **2006**, *74*, 140403.

(21) Liu, J.; del Barco, E.; Hill, S. Quantum Tunneling of Magnetization in Trigonal Single-Molecule Magnets. *Phys. Rev. B: Condens. Matter Mater. Phys.* **2012**, *85*, 012406.

(22) Henderson, J. J.; Koo, C.; Feng, P. L.; del Barco, E.; Hill, S.; Tupitsyn, I. S.; Stamp, P. C. E.; Hendrickson, D. N. Manifestation of

Spin Selection Rules on the Quantum Tunneling of Magnetization in a Single Molecule Magnet. *Phys. Rev. Lett.* **2009**, *103*, 017202.

(23) Liu, J.; del Barco, E.; Hill, S. A Microscopic and Spectroscopic View of Quantum Tunneling of Magnetization. In *Molecular Magnets—Physics and Applications*; Bartolomé, J., Luis, F., Fernández, J. F., Eds.; Springer Series on NanoScience and Technology; Springer-Verlag: Berlin, Heidelberg, 2014; pp 77−110.

(24) Marbey, J.; Gan, P.-R.; Yang, E.-C.; Hill, S. Magic angle effects in a trigonal Mn_3^{III} cluster: deconstruction of a single-molecule magnet. *Phys. Rev. B: Condens. Matter Mater. Phys.* **2018**, *98*, 144433.

(25) Affronte, M.; Troiani, F.; Ghirri, A.; Carretta, S.; Santini, P.; Corradini, V.; Schuecker, R.; Muryn, C.; Timco, G.; Winpenny, R. E. Molecular routes for spin cluster qubits. *Dalton Trans.* **2006**, 2810−2817.

(26) Zadrozny, J. M.; Xiao, D. J.; Atanasov, M.; Long, G. J.; Grandjean, F.; Neese, F.; Long, J. R. Magnetic blocking in a linear iron(I) complex. *Nat. Chem.* **2013**, *5*, 577−581.

(27) Ruamps, R.; Maurice, R.; Batchelor, L.; Boggio-Pasqua, M.; Guillot, R.; Barra, A. L.; Liu, J.; Bendeif, E.-E.; Pillet, S.; Hill, S.; Mallah, T.; Guihéry, N. Giant Ising-type magnetic anisotropy in trigonal Ni(II) complexes: experiment and theory. *J. Am. Chem. Soc.* **2013**, *135*, 3017−3026.

(28) Marriott, K. E. R.; Bhaskaran, L.; Wilson, C.; Medarde, M.; Ochsenbein, S. T.; Hill, S.; Murrie, M. Pushing the Limits of Magnetic Anisotropy in Trigonal Bipyramidal Ni(II). *Chem. Sci.* **2015**, *6*, 6823−6828.

(29) Woodruff, D. N.; Winpenny, R. E. P.; Layfield, R. A. Lanthanide Single-Molecule Magnets. *Chem. Rev.* **2013**, *113*, 5110−5148.

(30) Goodwin, C. A. P.; Ortu, F.; Reta, D.; Chilton, N. F.; Mills, D. P. Molecular magnetic hysteresis at 60 kelvin in dysprosocenium. *Nature* **2017**, *548*, 439−442.

(31) Guo, F.-S.; Day, B. M.; Chen, Y.-C.; Tong, M.-L.; Mansikkamäki, A.; Layfield, R. A. Magnetic hysteresis up to 80 kelvin in a dysprosium metallocene single-molecule magnet. *Science* **2018**, *362*, 1400−1403.

(32) Ding, Y.-S.; Chilton, N. F.; Winpenny, R. E. P.; Zheng, Y.-Z. On Approaching the Limit of Molecular Magnetic Anisotropy: A Near-Perfect Pentagonal Bipyramidal Dysprosium(III) Single-Molecule Magnet. *Angew. Chem. Int. Ed.* **2016**, *55*, 16071−16074.

(33) Giansiracusa, M. J.; Kostopoulos, A. K.; Collison, D.; Winpenny, R. E. P.; Chilton, N. F. Correlating Blocking Temperatures with Relaxation Mechanisms in Single-Molecule Magnets. *Chem. Commun.* **2019**, *55*, 7025−7028.

(34) Chiesa, A.; Cugini, F.; Hussain, R.; Macaluso, E.; Allodi, G.; Garlatti, E.; Giansiracusa, M.; Goodwin, C. A. P.; Ortu, F.; Reta, D.; Skelton, J. M.; Guidi, T.; Santini, P.; Solzi, M.; De Renzi, R.; Mills, D. P.; Chilton, N. F.; Carretta, S. Understanding magnetic relaxation in single-ion magnets with high blocking temperature. *Phys. Rev. B: Condens. Matter Mater. Phys.* **2020**, *101*, 174402.

(35) Velkos, G.; Krylov, D. S.; Kirkpatrick, K.; Spree, L.; Dubrovin, V.; Büchner, B.; Avdoshenko, S. M.; Bezmelnitsyn, V.; Davis, S.; Faust, P.; Duchamp, J.; Dorn, H. C.; Popov, A. A. High Blocking Temperature of Magnetization and Giant Coercivity in the Azafullerene $Tb_2@C_{79}N$ with a Single-Electron Terbium−Terbium Bond. *Angew. Chem. Int. Ed.* **2019**, *58*, 5891−5896.

(36) Liu, F.; Spree, L.; Krylov, D. S.; Velkos, G.; Avdoshenko, S. M.; Popov, A. A. Single-Electron Lanthanide-Lanthanide Bonds Inside Fullerenes toward Robust Redox-Active Molecular Magnets. *Acc. Chem. Res.* **2019**, *52*, 2981−2993.

(37) Sánchez, R. H.; Zheng, S.-L.; Betley, T. A. Ligand Field Strength Mediates Electron Delocalization in Octahedral $[(^{H}L)_2Fe_6(L')_m]^{n+}$ Clusters. *J. Am. Chem. Soc.* **2015**, *137*, 11126−11143.

(38) Sánchez, R. H.; Betley, T. A. Meta-Atom Behavior in Clusters Revealing Large Spin Ground States. *J. Am. Chem. Soc.* **2015**, *137*, 13949−13956.

(39) Sánchez, R. H.; Bartholomew, A. K.; Powers, T. M.; Ménard, G.; Betley, T. A. Maximizing Electron Exchange in a $[Fe_3]$ Cluster. *J. Am. Chem. Soc.* **2016**, *138*, 2235−2243.

(40) Greer, S. M.; McKay, J.; Gramigna, K. M.; Thomas, C. M.; Stoian, S. A.; Hill, S. Probing Fe-V Bonding in a C_3-Symmetric Heterobimetallic Complex. *Inorg. Chem.* **2018**, *57*, 5870−5878.

(41) Greer, S. M.; Gramigna, K. M.; Thomas, C. M.; Stoian, S. A.; Hill, S. Insights into Molecular Magnetism in Metal−Metal Bonded Systems as Revealed by a Spectroscopic and Computational Analysis of Diiron Complexes. *Inorg. Chem.* **2020**, *59*, 18141−18155.

(42) Barco, E. d.; Kent, A. D.; Hill, S.; North, J. M.; Dalal, N. S.; Rumberger, E. M.; Hendrickson, D. N.; Chakov, N.; Christou, G. Magnetic Quantum Tunneling in the Single Molecule Magnet Mn_{12}-Acetate. *J. Low Temp. Phys.* **2005**, *140*, 119−174.

(43) Hill, S. Magnetization tunneling in high-symmetry Mn_{12} single-molecule magnets. *Polyhedron* **2013**, *64*, 128−135.

(44) Redler, G.; Lampropoulos, C.; Datta, S.; Koo, C.; Stamatatos, T. C.; Chakov, N. E.; Christou, G.; Hill, S. Crystal lattice desolvation effects on the magnetic quantum tunneling of single-molecule magnets. *Phys. Rev. B: Condens. Matter Mater. Phys.* **2009**, *80*, 094408.

(45) Lampropoulos, C.; Murugesu, M.; Harter, A. G.; Wernsdofer, W.; Hill, S.; Dalal, N. S.; Reyes, A. P.; Kuhns, P. L.; Abboud, K. A.; Christou, G. Synthesis, Structure, and Spectroscopic and Magnetic Characterization of $[Mn_{12}O_{12}(O_2CCH_2Bu^t)_{16}(MeOH)_4]\cdot MeOH$, a Mn_{12} Single-Molecule Magnet with True Axial Symmetry. *Inorg. Chem.* **2013**, *52*, 258−272.

(46) Nehrkorn, J.; Holldack, K.; Bittl, R.; Schnegg, A. Recent Progress in Synchrotron-Based Frequency-Domain Fourier-Transform THz-EPR. *J. Magn. Reson.* **2017**, *280*, 10−19.

(47) Nehrkorn, J.; Martins, B. M.; Holldack, K.; Stoll, S.; Dobbek, H.; Bittl, R.; Schnegg, A. Zero-Field Splittings in MetHb and MetMb with Aquo and Fluoro Ligands: A FD-FTTHz-EPR Study. *Mol. Phys.* **2013**, *111*, 2696−2707.

(48) Schnegg, A.; Behrends, J.; Lips, K.; Bittl, R.; Holldack, K. Frequency Domain Fourier Transform THz-EPR on Single Molecule Magnets Using Coherent Synchrotron Radiation. *Phys. Chem. Chem. Phys.* **2009**, *11*, 6820−6825.

(49) Abo-Bakr, M.; Feikes, J.; Holldack, K.; Kuske, P.; Peatman, W. B.; Schade, U.; Wüstefeld, G.; Hübers, H.-W. Brilliant, Coherent Far-Infrared (THz) Synchrotron Radiation. *Phys. Rev. Lett.* **2003**, *90*, 094801.

(50) Hassan, A. K.; Pardi, L. A.; Krzystek, J.; Sienkiewicz, A.; Goy, P.; Rohrer, M.; Brunel, L.-C. Ultrawide Band Multifrequency High-Field EMR Technique: A Methodology for Increasing Spectroscopic Information. *J. Magn. Reson.* **2000**, *142*, 300−312.

(51) Mola, M.; Hill, S.; Goy, P.; Gross, M. Instrumentation for Millimeter-Wave Magnetoelectrodynamic Investigations of Low-Dimensional Conductors and Superconductors. *Rev. Sci. Instrum.* **2000**, *71*, 186−200.

(52) Takahashi, S.; Hill, S. Rotating Cavity for High-Field Angle-Dependent Microwave Spectroscopy of Low-Dimensional Conductors and Magnets. *Rev. Sci. Instrum.* **2005**, *76*, 023114.

(53) Komijani, D.; Ghirri, A.; Bonizzoni, C.; Klyatskaya, S.; Moreno-Pineda, E.; Ruben, M.; Soncini, A.; Affronte, M.; Hill, S. Radical-Lanthanide Ferromagnetic Interaction in a Tb^{III} Bis-Phthalocyaninato Complex. *Phys. Rev. Mater.* **2018**, *2*, 024405.

(54) Balasubramani, S. G.; Chen, G. P.; Coriani, S.; Diedenhofen, M.; Frank, M. S.; Franzke, Y. J.; Furche, F.; Grotjahn, R.; Harding, M. E.; Hättig, C.; Hellweg, A.; Helmich-Paris, B.; Holzer, C.; Huniar, U.; Kaupp, M.; Marefat Khah, A.; Karbalaei Khani, S.; Müller, T.; Mack, F.; Nguyen, B. D.; Parker, S. M.; Perlt, E.; Rappoport, D.; Reiter, K.; Roy, S.; Rückert, M.; Schmitz, G.; Sierka, M.; Tapavicza, E.; Tew, D. P.; van Wüllen, C.; Voora, V. K.; Weigend, F.; Wodyński, A.; Yu, J. M. TURBOMOLE: Modular program suite for ab initio quantum-chemical and condensed-matter simulations. *J. Chem. Phys.* **2020**, *152*, 184107.

(55) Becke, A. D. Density-functional thermochemistry. III. The role of exact exchange. *J. Chem. Phys.* **1993**, *98*, 5648−5652.

(56) Lee, C.; Yang, W.; Parr, R. G. Development of the Colle-Salvetti correlation-energy formula into a functional of the electron density. *Phys. Rev. B: Condens. Matter Mater. Phys.* **1988**, *37*, 785−789.

(57) Weigend, F.; Ahlrichs, R. Balanced basis sets of split valence, triple zeta valence and quadruple zeta valence quality for H to Rn: Design and assessment of accuracy. *Phys. Chem. Chem. Phys.* **2005**, *7*, 3297−3305.

(58) http://www.cgl.ucsf.edu/chimera/ (accessed September 2020).

(59) Nehrkorn, J.; Schnegg, A.; Holldack, K.; Stoll, S. General Magnetic Transition Dipole Moments for Electron Paramagnetic Resonance. *Phys. Rev. Lett.* **2015**, *114*, 10801.

(60) Stoll, S.; Schweiger, A. EasySpin, a Comprehensive Software Package for Spectral Simulation and Analysis in EPR. *J. Magn. Reson.* **2006**, *178*, 42−55.

(61) Nehrkorn, J.; Telser, J.; Holldack, K.; Stoll, S.; Schnegg, A. Simulating Frequency-Domain Electron Paramagnetic Resonance: Bridging the Gap between Experiment and Magnetic Parameters for High-Spin Transition-Metal Ion Complexes. *J. Phys. Chem. B* **2015**, *119*, 13816−13824.

(62) Rudowicz, C.; Chung, C. Y. The generalization of the extended Stevens operators to higher ranks and spins, and a systematic review of the tables of the tensor operators and their matrix elements. *J. Phys.: Condens. Matter* **2004**, *16*, 5825−5847.

(63) Krzystek, J.; Ozarowski, A.; Telser, J. Multi-Frequency, High-Field EPR as a Powerful Tool to Accurately Determine Zero-Field Splitting in High-Spin Transition Metal Coordination Complexes. *Coord. Chem. Rev.* **2006**, *250*, 2308−2324.

(64) Hay, M. A.; Sarkar, A.; Craig, G. A.; Bhaskaran, L.; Nehrkorn, J.; Ozerov, M.; Marriott, K. E. R.; Wilson, C.; Rajaraman, G.; Hill, S.; Murrie, M. In-depth investigation of large axial magnetic anisotropy in monometallic 3d complexes using frequency domain magnetic resonance and ab initio methods: a study of trigonal bipyramidal Co(II). *Chem. Sci.* **2019**, *10*, 6354−6361.

(65) Hill, S.; Anderson, N.; Wilson, A.; Takahashi, S.; Petukhov, K.; Chakov, N. E.; Murugesu, M.; North, J. M.; Barco, E. d.; Kent, A. D.; Dalal, N. S.; Christou, G. A comparison between high-symmetry Mn_{12} single-molecule magnets in different ligand/solvent environments. *Polyhedron* **2005**, *24*, 2284−2292.

(66) Chakov, N. E.; Lee, S.-C.; Harter, A. G.; Kuhns, P. L.; Reyes, A. P.; Hill, S. O.; Dalal, N. S.; Wernsdorfer, W.; Abboud, K. A.; Christou, G. The Properties of the $[Mn_{12}O_{12}(O_2CR)_{16}(H_2O)_4]$ Single-Molecule Magnets in Truly Axial Symmetry: $[Mn_{12}O_{12}(O_2CCH_2Br)_{16}(H_2O)_4]\cdot CH_2Cl_2$. *J. Am. Chem. Soc.* **2006**, *128*, 6975−6989.

(67) Barra, A.-L.; Caneschi, A.; Cornia, A.; Gatteschi, D.; Gorini, L.; Heiniger, L.-P.; Sessoli, R.; Sorace, L. The Origin of Transverse Anisotropy in Axially Symmetric Single Molecule Magnets. *J. Am. Chem. Soc.* **2007**, *129*, 10754−10762.

(68) Maccagnano, S.; Achey, R.; Negusse, E.; Lussier, A.; Mola, M. M.; Hill, S.; Dalal, N. S. Single crystal EPR determination of the spin Hamiltonian parameters for Fe_8 molecular clusters. *Polyhedron* **2001**, *20*, 1441−1445.

(69) Park, K.; Novotny, M. A.; Dalal, N. S.; Hill, S.; Rikvold, P. A. Effects of D-strain, g-strain, and dipolar interactions on EPR Linewidths of the Molecular Magnets Fe_8 and Mn_{12}. *Phys. Rev. B: Condens. Matter Mater. Phys.* **2001**, *65*, 014426.

(70) Hill, S.; Maccagnano, S.; Park, K.; Achey, R. M.; North, J. M.; Dalal, N. S. Detailed single crystal EPR line shape measurements for the single molecule magnets Fe_8Br and Mn_{12}−acetate. *Phys. Rev. B: Condens. Matter Mater. Phys.* **2002**, *65*, 224410.

(71) Hill, S.; Edwards, R. S.; Jones, S. I.; Dalal, N. S.; North, J. M. Definitive spectroscopic determination of the transverse interactions responsible for the magnetic quantum tunneling in Mn_{12}-acetate. *Phys. Rev. Lett.* **2003**, *90*, 217204.

(72) Takahashi, S.; Edwards, R. S.; North, J. M.; Hill, S.; Dalal, N. S. Discrete easy-axis tilting in Mn_{12}-acetate, as determined by EPR: implications for the magnetic quantum tunneling mechanism. *Phys. Rev. B* **2004**, *70*, 094429.

(73) Graham, M. J.; Zadrozny, J. M.; Fataftah, M. S.; Freedman, D. E. Forging Solid-State Qubit Design Principles in a Molecular Furnace. *Chem. Mater.* **2017**, *29*, 1885−1897.

(74) Marbey, J.; Gan, P.-R.; Yang, E.-C.; Hill, S. Magic angle effects in a trigonal Mn_3^{III} cluster: deconstruction of a single-molecule magnet. *Phys. Rev. B: Condens. Matter Mater. Phys.* **2018**, *98*, 144433.

(75) Foss-Feig, M. S.; Friedman, J. R. Geometric-Phase-Effect Tunnel-Splitting Oscillations in Single-Molecule Magnets with Fourth-Order Anisotropy Induced by Orthorhombic Distortion. *Europhys. Lett.* **2009**, *86*, 27002.

(76) Bencini, A.; Gatteschi, D. *Electron Paramagnetic Resonance of Exchange Coupled Systems*; Springer-Verlag: Berlin, Heidelberg, 1990.

(77) Datta, S.; Bolin, E.; Inglis, R.; Milios, C. J.; Brechin, E. K.; Hill, S. A comparative EPR study of high- and low-spin Mn_6 single molecule magnets. *Polyhedron* **2009**, *28*, 1788−1791.

(78) Lawrence, J.; Yang, E.-C.; Hendrickson, D. N.; Hill, S. Magnetic Quantum Tunneling: Key Insights from Multi-Dimensional High-Field EPR. *Phys. Chem. Chem. Phys.* **2009**, *11*, 6743−6749.

(79) Lampropoulos, C.; Hill, S.; Christou, G. A Caveat for Single-Molecule Magnetism: Nonlinear Arrhenius Plots. *ChemPhysChem* **2009**, *10*, 2397−2400.

(80) Hill, S.; Murugesu, M.; Christou, G. Anisotropy barrier reduction in fast-relaxing Mn_{12} single-molecule magnets. *Phys. Rev. B: Condens. Matter Mater. Phys.* **2009**, *80*, 174416.

(81) *Metal-Metal Bonding*; Parkin, G., Ed.; Structure and Bonding; Springer: Berlin,Heidelberg, 2010; Vol. *136*.

(82) Chakarawet, K.; Bunting, P. C.; Long, J. R. Large Anisotropy Barrier in a Tetranuclear Single-Molecule Magnet Featuring Low-Coordinate Cobalt Centers. *J. Am. Chem. Soc.* **2018**, *140*, 2058−2061.

(83) Chakarawet, K.; Atanasov, M.; Marbey, J.; Bunting, P. C.; Neese, F.; Hill, S.; Long, J. R. Strong Electronic and Magnetic Coupling in M_4 (M = Ni, Cu) Clusters via Direct Orbital Interactions Between Low-Coordinate Metal Centers. *J. Am. Chem. Soc.* **2020**, *142*, 19161−19169.